Advanced Materials Interfaces

ADVANCED MATERIALS INTERFACES Open Access

www.advmatinterfaces.de

RESEARCH ARTICLE OPEN ACCESS

Enhanced Thermal Conductivity in Tough and Environmentally Resilient Hydrogels

Seokkyoon Hong[1] | Jiwon Lee[2] | Taewoong Park[1] | Jinheon Jeong[1] | Hyeonseo Joo[1,2] | Juan C. Mesa[1,3,4] | Claudia Benito Alston[1] | Yuhyun Ji[1] | Jonghun Yi[2] | Youngjun Lee[1] | Kate J. Won[1] | Luis Solorio[1] | Young L. Kim[1] | Hyowon Lee[1,3,4] | Dong Rip Kim[2] | Chi Hwan Lee[1,3,4,5,6,7]

[1]Weldon School of Biomedical Engineering, Purdue University, West Lafayette, Indiana, USA | [2]School of Mechanical Engineering, Hanyang University, Seoul, Republic of Korea | [3]Center for Implantable Devices, Purdue University, West Lafayette, Indiana, USA | [4]Birck Nanotechnology Center, Purdue University, West Lafayette, Indiana, USA | [5]Elmore Family School of Electrical and Computer Engineering, Purdue University, West Lafayette, Indiana, USA | [6]School of Mechanical Engineering, Purdue University, West Lafayette, Indiana, USA | [7]School of Materials Engineering, Purdue University, West Lafayette, Indiana, USA

Correspondence: Dong Rip Kim (dongrip@hanyang.ac.kr) | Chi Hwan Lee (lee2270@purdue.edu)

Received: 19 August 2025 | **Revised:** 24 November 2025 | **Accepted:** 30 November 2025

Keywords: biomimetic materials | hierarchical structures | hydrogels | thermal conductivity | wearable sensors

ABSTRACT

Hydrogels, known for their biocompatibility and responsiveness to external stimuli, are promising candidates for wearable sensors and electronics. However, conventional hydrogels exhibit low thermal conductivity (0.2–0.6 W/m·K), which limits efficient heat dissipation and leads to performance degradation during continuous operation, such as in long-term wearable health monitors. Moreover, their weak mechanical and environmental stability further constrains their broader applications. In this study, we introduce a multiscale structural engineering approach that leverages the dynamics of pores, crystallization, and hydrogen bonding. Inspired by the design motifs of natural materials such as spider silk, we enhance the thermal conductivity of hydrogels to 1.5 W/m·K. This multiscale structural strategy also improves their mechanical strength and environmental resilience. Our findings provide a blueprint for understanding the process–structure–property relationships and offer a design framework for expanding the practical applications of hydrogels.

1 | Introduction

Hydrogels are widely used in advanced technologies, such as wearable sensors and electronics due to their biocompatibility and responsiveness to external stimuli [1–10]. However, their application in wearable sensing is challenged by poor thermal management, as well as limited mechanical and environmental stability. In particular, the low thermal conductivity (0.2–0.6 W/m·K) poses a significant challenge, limiting heat dissipation and overall performance [11]. This limited heat dissipation capacity poses challenges in thermal management, for long-term use in wearable sensors such as health monitors and flexible electronics [12].

Several strategies have been proposed to address the thermal conductivity limitations of hydrogels. One common approach to enhance thermal conductivity is the addition of high-conductivity fillers, such as metal (e.g., silver and copper) [13, 14] or ceramic (e.g., boron nitride and aluminum oxide) [15–17] particles. Yet, this method increases material cost and weight. Another strategy involves strengthening intermolecular interactions, which typically focuses on single-scale modifications (e.g., nano- or molecular-levels)[18–27]. While this approach has shown improved thermal conductivity (e.g., 0.64–1.23 W/m•K), it still leaves room for further enhancement through multiscale structural engineering [18–27]. Moreover, the weak intermolecular interactions in hydrogels contribute to limited mechanical

---

strength and environmental stability, both of which are crucial for reliable and durable wearable sensor applications [28–30].

Nature has perfected extraordinary materials such as spider silk, known for its exceptional thermal conductivity, mechanical strength, and environmental resilience [31, 32]. These remarkable characteristics are largely derived from its hierarchical structure across multiple length scales [33, 34]. For example, Gu et al. demonstrated that the toughness of spider silk is governed by β-nanocrystalline domains reinforced by dense hydrogen-bond networks [35]. Fu et al. demonstrated that the cryogenic toughness of spider silk originates from its well-defined micro- and nanofibrillar morphology, which blunts crack propagation, and from the highly oriented chain structures within the nanofibrils that enable substantial elastic energy absorption through ordered–disordered chain deformation [32]. Huang et al. attributed the high thermal conductivity of dragline silk to well-organized and low-defect structures of protein chains and aligned β-sheet nanocrystals that promote efficient phonon transport [36]. Atomistic simulations further confirm that densely packed β-sheet crystals and extensive hydrogen-bond networks enhance heat transfer at the molecular level [33]. Biomimicking the design principles of spider silk could enable the development of hydrogels with significantly improved thermal conductivity, broadening their range of potential applications.

In this study, inspired by the structural motifs of spider silk, we engineered multiscale structures within hydrogel to achieve enhanced performance. The hydrogels demonstrate superior thermal conductivity of 1.5 W/m·K, impressive compressive strength of 5.4 MPa, and toughness of 1.1 MJ m^{-3}, along with exceptional environmental tolerance across diverse conditions, from −150°C to 70°C, under 12 psi, and after one month of ambient storage. These advanced features result from strategic multiscale structural modifications that improve 1) compactness at the microscale, 2) crystallinity and crystallite size at the nanoscale, and 3) hydrogen bonding at the molecular scale. The multiscale engineering approach presented in this study simultaneously enhances the thermal conductivity, along with mechanical strength and environmental resilience (Scheme 1). This study offers innovative material design guidelines, elucidating the mechanisms linking hierarchical structures to enhanced performance.

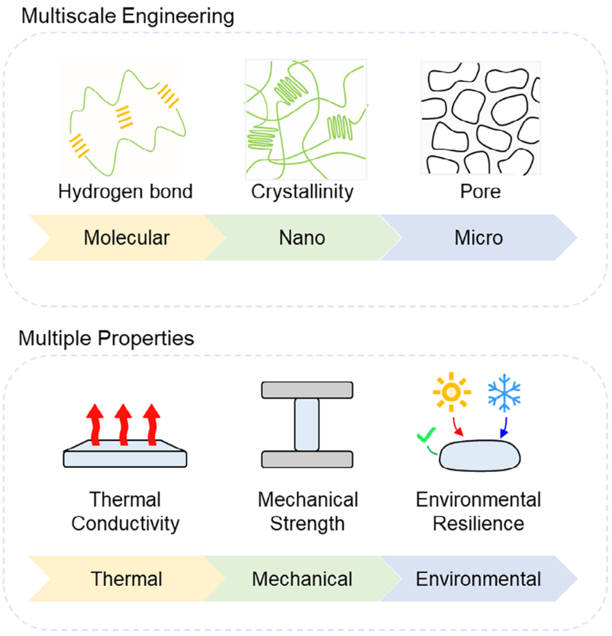

SCHEME 1 | Multiscale engineered hydrogels for enhanced thermal conductivity with improved mechanical strength and environmental resilience.

2 | Results and Discussion

2.1 | Enhanced Thermal Conductivity via Multiscale Engineering

Spider silk is known for its exceptional thermal conductivity, attributed to its nearly defect-free structures, β-sheet crystals, and extensive hydrogen bonding [34]. Drawing inspiration from this, we applied multiscale structural engineering to conductive hydrogels, utilizing solvent engineering (SE-Hydrogel) and dry annealing (DA-Hydrogel) of a standard hydrogel (ST-Hydrogel). This approach promotes hierarchically compact structures across micro-, nano-, and molecular levels. To investigate how thermal conductivity can be enhanced, we synthesized three types of hydrogels such as ST-, SE-, and DA-Hydrogels, following detailed procedures described in the Experimental Section (Figure S1). DA-Hydrogels were synthesized through a combination of freeze-thawing and dry-annealing processes (Figure S2). A solution was prepared by vigorous mechanical mixing, followed by freeze-thawing to induce physical crosslinking of PEDOT-rich crystalline domains and hydrogen-bonded PVA crystalline domains, imparting conductivity and stretchability, respectively, to generate ST-Hydrogel and SE-Hydrogel, depending on the solvent type. Subsequent dry annealing facilitated the formation of dense hierarchical structures across micro-, nano-, and molecular-levels to create the DA-Hydrogel. The fabrication process is described in detail in the Experimental Section. Among these, DA-Hydrogels exhibited the highest thermal conductivity of 1.5 W/m·K, compared to 1.0 W/m·K for ST-Hydrogels and 1.2 W/m·K for SE-Hydrogels (Figure 1a). Thermal conductivity measurements were conducted using a 1D steady-state method, with specifics outlined in the Experimental Section (Figure S3a). The temperature profiles over time for the three hydrogel types are depicted in Figure S3b. To visually represent these differences, hydrogels were placed on a hot plate at 80°C, and an infrared (IR) camera captured the in situ temperature distribution. DA-Hydrogels demonstrated a faster temperature increase along the Z-direction compared to ST- and SE-Hydrogels, confirming the superior thermal conductivity of DA-Hydrogels (Figure 1b). Furthermore, IR imaging provides clear evidence of higher thermal conductivity of DA-Hydrogels, as indicated by their higher temperature distribution relative to ST- and SE-Hydrogels after 12 min of heating (Figure 1c; Movie S1).

The mechanisms underlying the enhanced thermal conductivity were systematically analyzed across multiple scales, providing insights into how microstructural compactness, crystallinity, and strengthened hydrogen bonding collectively contribute to performance improvements in hydrogels (Figure 1d; Figure S4). At the microscale (> 1 µm), pore dynamics were examined using scanning electron microscopy (SEM) (Figure 1d, top row).

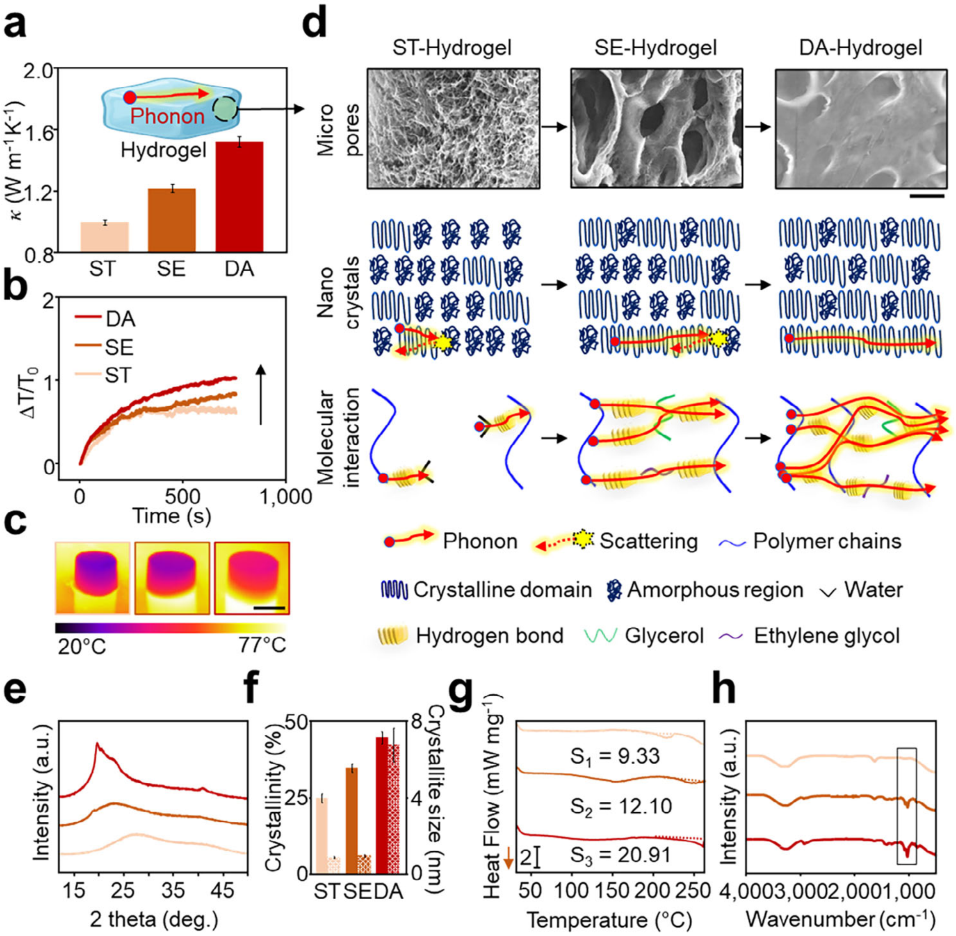

FIGURE 1 | Enhanced thermal conductivity. (a) Thermal conductivities of ST-, SE-, and DA-Hydrogels. Data presented as mean ± SD, n = 3. (b) Plots of $\Delta T/T_0$ versus time for ST-, SE-, and DA-Hydrogels. (c) IR images of ST-, SE-, and DA-Hydrogels. Scale bar, 1 cm. (d) Thermal transport analysis of ST-, SE-, and DA-Hydrogels at multi-scales. Scale bar, 50 µm. (e) XRD analysis of ST-, SE-, and DA-Hydrogels. (f) Crystallinity and crystallite size of ST-, SE-, and DA-Hydrogels. Data presented as mean ± SD, n = 3. (g) DSC analysis of ST-, SE-, and DA-Hydrogels. (h) FTIR spectra of ST-, SE-, and DA-Hydrogels.

ST-Hydrogels, composed primarily of water, exhibit a network of pores supported by thin polymer backbones. The introduction of organic solvents densifies the structure in SE-Hydrogel through increased intermolecular interactions [37], while dry annealing further tightens molecular chain alignment and closes pores [38]. These modifications reduce the number of pores, which serve as phonon scattering sites, thereby enhancing thermal conductivity (Figures S5 and S6) [39, 40].

Crystallization dynamics were investigated at the nanoscale (1 nm to 1 µm) (Figure 1d, middle row). X-ray diffraction (XRD) reveals a sharp peak at $2\theta \approx 19.7°$, indicating the crystallinity of polyvinyl alcohol (PVA) chains (Figure 1e,f) [41]. ST-Hydrogel shows the lowest crystallinity (24.9%) and crystallite size (0.88 nm), whereas SE-Hydrogel exhibits increased crystallinity (34.9%) and crystallite size (0.98 nm) due to enhanced chain mobility in the supercooled state, which facilitates the formation of more ordered PVA structures promoted by organic solvents [42]. Dry annealing further enhances crystallinity to 44.7% and crystallite size up 6.7 nm by promoting PVA chain alignment through increased chain mobility (Figure 1e,f) [43], thereby reducing amorphous regions that act as phonon scattering centers [26, 44]. Differential scanning calorimetry (DSC) analysis further demonstrates that the DA-Hydrogel exhibits a larger area of the endothermic melting peak area compared to the ST-Hydrogel and SE-Hydrogel, reflecting a greater number of crystalline domains in the DA-Hydrogel (Figure 1g).

Intermolecular interactions at the molecular scale (< 1 nm) were analyzed using Fourier transform infrared (FTIR) spectroscopy (Figure 1d, bottom row, Figure 1h). The C—O stretching band at 1089 cm^{-1} in ST-Hydrogel shifts to lower wave numbers (1038 and 1035 cm^{-1}) in SE- and DA-Hydrogels, indicating stronger hydrogen bonding (Figure S7a) [45]. Additionally, DA-Hydrogel shows an intensified crystal-sensitive band at 1144 cm^{-1}, reflecting enhanced PVA crystallization and stronger intermolecular interactions compared to ST- and SE-Hydrogels (Figure S7b) [46]. These strengthened hydrogen bonds eliminate gaps within the DA-Hydrogel, further reducing phonon scattering centers and enhancing thermal conductivity [24]. The thermal conductivity increases with the decreased water content and then reaches a plateau thereafter (Figure S8). In conclusion, multiscale structural changes, including 1) reduced voids at the microscale, 2) increased crystalline regions at the nanoscale, and 3) strengthened intermolecular interactions at the molecular scale, work synergistically to improve thermal conductivity, surpassing the thermal conductivity of previously reported single- or dual-scale approaches or materials with low-water-content (Figure S9; Tables S1 and S2) [18–27, 47–50].

2.2 | Strong yet Lightweight Hydrogels

Many applications, such as wearable devices and soft robotics, require materials with high mechanical performance to ensure long-term durability [28]. At the same time, low density is essential to maintain the agility of moving components and enhance user comfort [51]. However, hydrogels often suffer from limited mechanical strength and high density due to their high water content [51, 52]. Consequently, the development of mechanically robust and lightweight hydrogels is of great importance.

By employing compact structuring across micro-, nano-, and molecular scales, DA-Hydrogels demonstrate outstanding mechanical strength. Specifically, DA-Hydrogels exhibit 1) reduced voids at the microscale, 2) increased crystalline regions and crystallinity at the nanoscale, and 3) strengthened hydrogen bonding at the molecular scale. This hierarchical multiscale compactness in hydrogels significantly enhances the mechanical properties of DA-Hydrogels compared to ST- and SE-Hydrogels, as demonstrated in Figure 2a and Figure S10.

To illustrate the enhanced mechanical properties, a 13.6 kg dumbbell (1360 times the hydrogel's own weight) was placed on ST-, SE-, and DA-Hydrogels. While ST- and SE-Hydrogels exhibited pronounced deformation under this load, DA-Hydrogels maintained their structural integrity with minimal deformation (Figure 2b). This remarkable load-bearing capacity is attributed to synergistic effects from enhanced crystallinity, increased crystallite size, and strengthened hydrogen bonding, coupled with compact microstructures, as depicted schematically in Figure 2c. The multiscale toughening and strengthening strategy enabled the DA-Hydrogel to support an even greater load of 45.4 kg (1892 times its weight) without mechanical failure (Figure 2d; Movie S2). Such exceptional mechanical robustness originates from dynamic interactions operating across multiple length scales, including compact microstructures, enhanced nanocrystallization, and strengthened intermolecular interactions. As a result, the combined effects of reduced voids, enhanced crystallinity and crystallite size, and strengthened hydrogen bonding led to significant improvements in compressive mechanical strength, modulus, and toughness, surpassing the performance of previously developed tough hydrogels (Figure S11) [53–58].

DA-Hydrogels exhibit a remarkably lightweight nature, primarily due to water evaporation during the dry annealing process. This weight reduction enables them to rest stably on a single leaf of a pencil cactus, visually demonstrating their low density (Figure 2e). This water evaporation is supported by FTIR analysis, which shows a decreased intensity of the peak at 1645 cm^{-1} corresponding to the bending vibration of hydroxyl groups (δ (−OH, H_2O)), associated with bound water (Figure 2f) [46]. Peaks corresponding to the bending vibration of hydroxyl groups (δ(−OH, H_2O)) at 1645 cm^{-1}, which are attributed to bound water, are still observed even after dry annealing (Figure 2f). This observation indicates that the residual bound water cannot be completely removed, thereby confirming the persistence of the hydrogel network structure. DA-Hydrogels achieve the lowest density due to water evaporation, and ST-Hydrogels have lower density than SE-Hydrogels since water is less dense than organic solvents (Figure 2g). This unique combination of low density and enhanced mechanical performance enables DA-Hydrogels to achieve the highest specific mechanical properties compared to ST- and SE-Hydrogels (Figure 2h, Figure S12).

2.3 | Mechanical Stability and Recovery

Ensuring mechanical stability and recovery is crucial for the long-term durability and functionality of conductive hydrogels under repetitive or extreme stresses [59]. The compressibility and self-recovery of DA-Hydrogels were evaluated using cylindrical specimens subjected to 50% compressive strain. The DA-Hydrogel demonstrated rapid recovery to its original shape upon unloading (Figure 3a). Compressive loading-unloading cycles at 50% strain were conducted on ST-, SE-, and DA-Hydrogels to assess energy dissipation (Figure 3b). DA-Hydrogels exhibited superior energy dissipation, attributed to crystalline domains and dense hydrogen bonding that unzip and release mechanical energy. This structural configuration allows DA-Hydrogels to dissipate more energy than ST- and SE-Hydrogels, as evidenced by significant energy dissipation and a higher energy dissipation coefficient during the initial cycle (Figure S13).

The cyclic compressive tests reveal that the DA-Hydrogel maintains consistent hysteresis loops beyond the first cycle, demonstrating rapid self-recovery and excellent fatigue resistance (Figure 3c). The stable energy dissipation coefficient (U_{hys} coefficient) and preserved stress levels underscore the hydrogel's durability (Figure 3d). DA-Hydrogels also show increased hysteresis energy with higher strain levels, attributed to the gradual destruction of crystalline domains and hydrogen bonds, maintaining higher energy dissipation and stress compared to ST- and SE-Hydrogels (Figure 3e; Figure S14). Even after 1000 loading/unloading cycles at 50% strain, DA-Hydrogels retain exceptional fatigue resistance and durability (Figure 3f). Extreme compressibility and recoverability were further demonstrated through human and vehicle compression tests. The hydrogel withstood a 70 kg person standing on it for 1 min (Figure 3g) and endured repeated compression by a 1500 kg vehicle (Figure 3h; Movie S3), showing complete recovery with no fractures or permanent deformation (Figure 3h; Figure S15). Additionally, cutting deformation tests showed that DA-Hydrogels resist high localized stress without visible damage, further illustrating their toughness and self-recovery (Figure 3i; Movie S4). These findings highlight the exceptional compressibility, energy dissipation, and recoverability of DA-Hydrogels, making them ideal for applications subjected to extreme mechanical stresses.

2.4 | Environmental Stability

Hydrogels often suffer from limited environmental stability, restricting their usability in varying conditions [8, 60–62]. Regarding the environmental stability, we conducted various

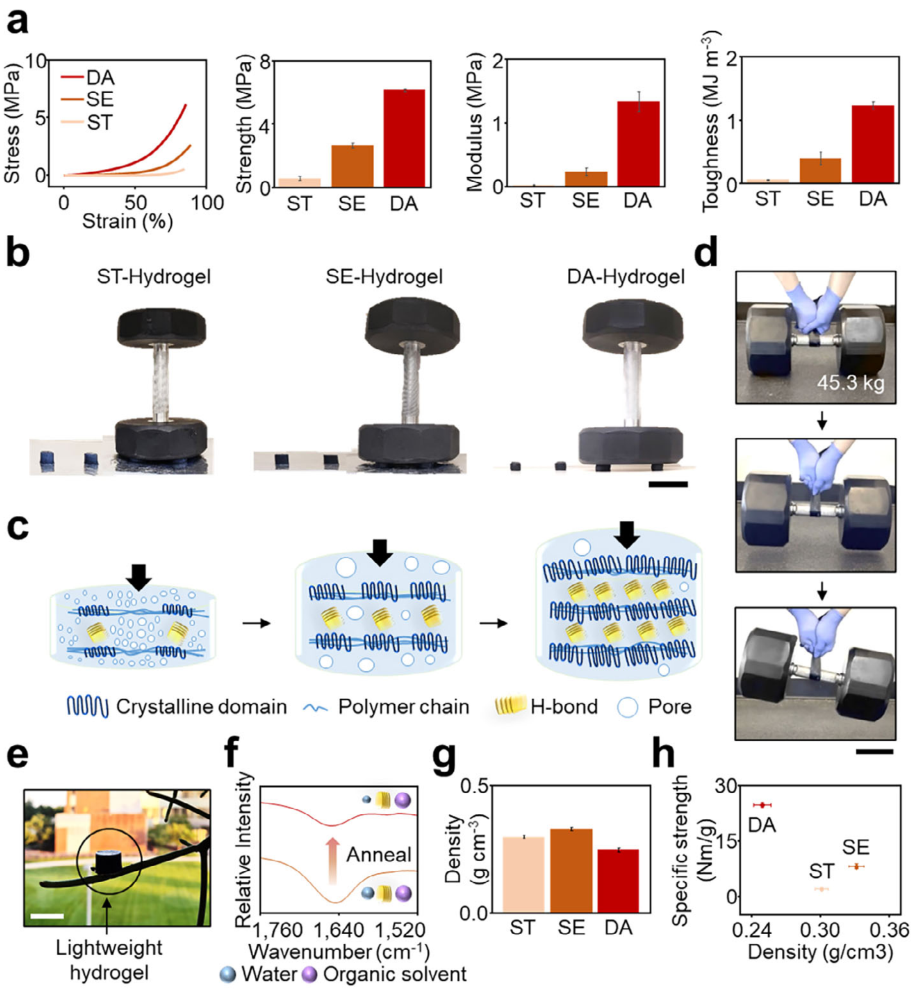

FIGURE 2 | Enhanced specific mechanical properties. (a) Compressive stress–strain curves and mechanical properties (e.g., strength, modulus, and toughness) of ST-, SE-, and DA-Hydrogels. Data presented as mean ± SD, n = 3. (b) Comparison of deformation in ST-, SE-, and DA-Hydrogels under a 13.6 kg load. Scale bar, 6 cm. (c) Multiscale strengthening and toughening mechanism of the DA-Hydrogel. (d) DA-Hydrogel, supporting the weight of a 45.3 kg dumbbell. Scale bar, 20 cm. (e) Photograph of DA-Hydrogel positioned on a leaf. Scale bar, 2 cm. (f) FTIR spectra of hydrogels before and after annealing. (g) Density of ST-, SE-, and DA-Hydrogels. Data presented as mean ± SD, n = 3. (h) Specific strength versus density of ST-, SE-, and DA-Hydrogels. Data presented as mean ± SD, n = 3.

environmental stability tests and DA-Hydrogels achieved exceptional stability through multiscale structural engineering. For example, the anti-drying properties were tested by tracking weight changes over 30 days at room temperature. DA-Hydrogels exhibited minimal weight loss, indicating strong resistance to drying, attributed to their dense structure and robust intermolecular interactions, while ST- and SE-Hydrogels showed significant weight reduction under the same conditions (Figure 4a). The anti-freezing capabilities of DA-Hydrogels are also remarkable, due to these strong interactions. DSC measurements from −150°C to 50°C showed a sharp peak at 3.8°C for ST-Hydrogels, corresponding to water freezing. In contrast, DA-Hydrogels displayed no significant freezing peaks, underscoring the improved freeze resistance (Figure 4b). DA-Hydrogels retained compressibility at −20°C, unlike ST-Hydrogels, which fractured when hammered at this temperature (inset in Figure 4b), demonstrating superior freeze resistance compared to conventional hydrogels (Figure S16) [60, 61, 63]. Further environmental tests at temperatures ranging from −20°C to 70°C and under vacuum (12 psi) revealed negligible weight variation over 12 h, confirming DA-Hydrogels' robust tolerance, except at 120°C (Figure 4c). The compressive stress–strain curves remained consistent across these conditions, affirming excellent stability (Figure 4d). The DA-Hydrogel maintained impressive compressive stress under diverse conditions, as demonstrated by its capacity to support a 500 g weight (Figure 4e). The DA-Hydrogel also retained its toughness across diverse environmental conditions, further underscoring its robustness (Figure 4f). Similarly, tensile stress–strain curves demonstrated environmental stability, supporting the hydrogel's reliability in diverse environments (Figure S17). These findings highlight how multiscale structural engineering enhances both mechanical properties and environmental resilience.

2.5 | Strain Sensing Performance

The combination of superior mechanical properties and environmental resilience makes DA-Hydrogels well-suited for strain sensing. The hydrogels exhibit highly linear relative resistance

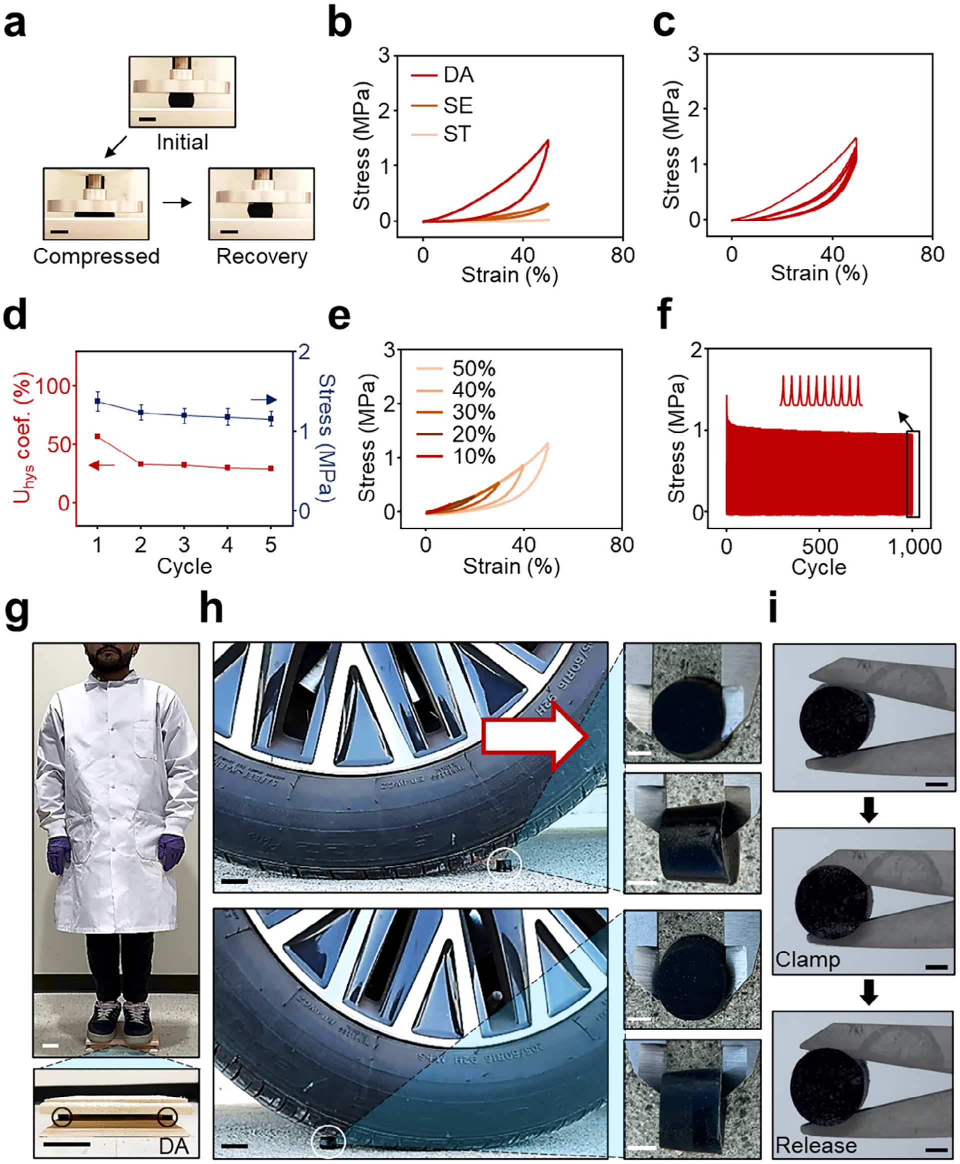

FIGURE 3 | Mechanical stability and recovery. (a) Photographs of compression and self-recovery of the DA-Hydrogel. Scale bar, 1 cm. (b) Compressive stress–strain curves for ST-, SE-, and DA-Hydrogels. (c) Cyclic stress–strain curves for DA-Hydrogels. (d) The evolution of energy loss coefficient and compressive stress as a function of loading-unloading cycles. Data presented as mean ± SD, n = 3. (e) Compressive stress–strain curves of DA-Hydrogels at different strains. (f) Compressive stress of the DA-Hydrogel throughout 1000 loading-unloading cycles. (g) Photographs, showing the compressive strength of the DA-Hydrogel under the 70 kg human load. Scale bar, 5 cm. (h) Photographs of a car compression test demonstrating the DA-Hydrogel subjected to a compressive force of 1500 kg from a car over 5 consecutive cycles. Scale bar, 3 cm. Enlarged photographs, showing DA-Hydrogels before and after car compression testing. Scale bar, 5 mm. (i) Photographs of the DA-Hydrogel cut with scissors. Scale bar, 5 mm.

changes ($\Delta R/R_0$) under compressive strain across varied environmental conditions ($R^2 > 0.98$), including a broad temperature range (−20 to 70°C), vacuum conditions (12 psi), and extended storage (1-month in ambient conditions) (Figure 5a). The hydrogels demonstrate a gauge factor exceeding 0.25, ensuring consistent and reliable pressure sensing performance (Figure 5b). Similarly, the hydrogels exhibit stable electrical sensing under tensile strain with high linearity ($R^2 > 0.99$) and a gauge factor exceeding 0.30 across diverse environments (Figure S18). Figure 5c illustrates the $\Delta R/R_0$ response of the DA-Hydrogel subjected to 50% compressive strain during loading-unloading cycles across various conditions. The response patterns remained consistent under all tested environmental conditions, underscoring its remarkable environmental resilience and durability. Figure 5d shows the $\Delta R/R_0$ response of the DA-Hydrogel during loading-unloading cycles at varying strain levels (10%, 30%, and 50%). The consistent response patterns observed at various compressive strain levels underscore the stability and reliable performance of the DA-hydrogels, demonstrating continuous and repeatable responses during cyclic loading. The consistency is sustained over 1000 cycles of compressive strains of 50%, further demonstrating the DA-Hydrogel's stability and enduring performance without any signs of failure (Figure 5e). Figure 5f presents the response and recovery times of the DA-Hydrogel under the compressive

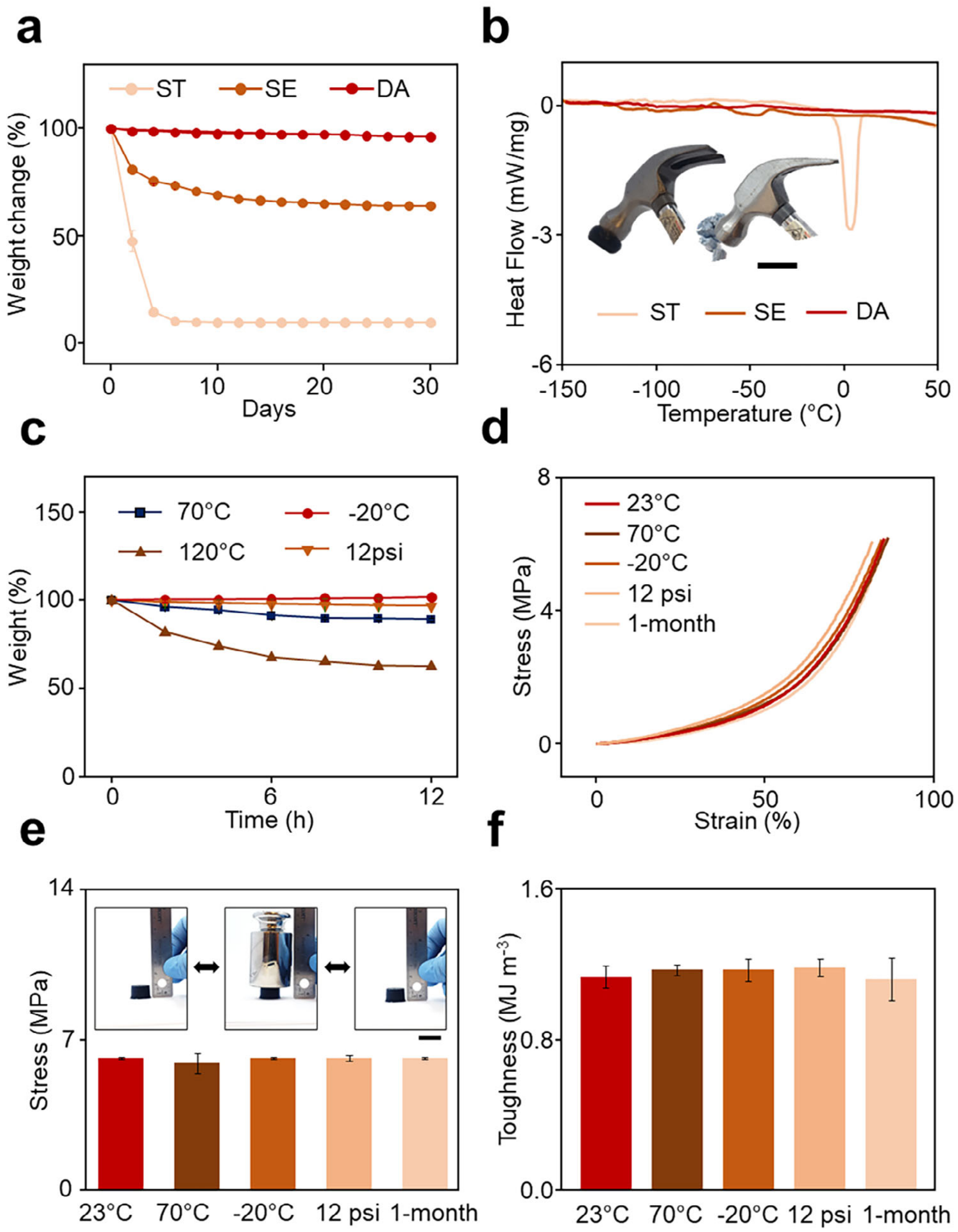

FIGURE 4 | Environmental stability. (a) Weight change of ST-, SE-, and DA-Hydrogels for 1-month storage. Data presented as mean ± SD, n = 3. (b) DSC curves of ST-, SE-, and DA-Hydrogels. Inset: Images of hammering ST- and DA-Hydrogels after freezing. Scale bar, 2 cm. (c) Weight change of DA-Hydrogels under various environments. Data presented as mean ± SD, n = 3. (d) Compressive stress–strain curves of DA-Hydrogels under various environments. (e) Compressive stress of the DA-Hydrogel under diverse conditions. Inset: Images of DA-Hydrogels under a 500 g load. Scale bar, 2 cm. Data presented as mean ± SD, n = 3. (f) Toughness of the DA-Hydrogel across various environments. Data presented as mean ± SD, n = 3.

strain of 50%, with a loading and unloading rate of 500 mm min^{-1}. The DA-Hydrogel demonstrated response and recovery times without notable deviations under 50% compressive strain with the response and recovery times of approximately 725 and 922 ms.

2.6 | Proof-Of-Concept Demonstrations in Wearable Sensing

Achieving environmental tolerance while maintaining strain sensing performance and thermal management in the hydrogel is essential for wearable sensing to broaden their utilization [24, 64–68]. In this regard, our hydrogel uniquely possesses the combination of strain sensing, thermal management, and environmental resilience. To demonstrate both thermal management and strain sensing capabilities, ST-, SE-, and DA-Hydrogels were tested on a hot plate maintained at 70 °C. After thermal equilibrium was reached, the hydrogels were transferred to a clean surface at room temperature. The DA-Hydrogel exhibited the fastest temperature decrease (30.3%) compared to SE-Hydrogel (25.3%) and ST-Hydrogel (20%), owing to its hierarchically compact structure, which significantly enhances thermal conductivity (Figure 6a). Pressure sensing performance was evaluated by subjecting the hydrogels to repeated pressing and releasing motions. Both DA- and SE-Hydrogels successfully

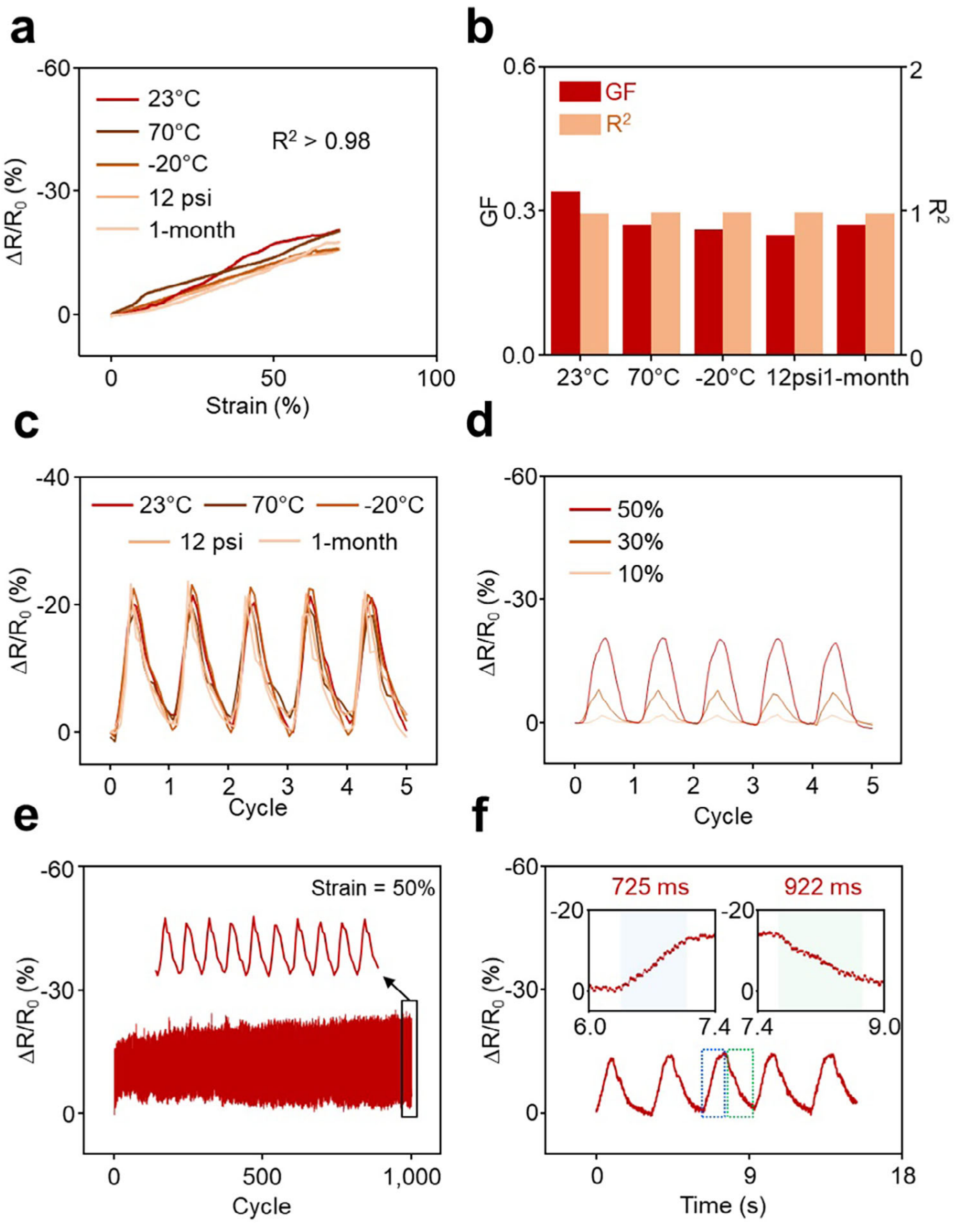

FIGURE 5 | Strain sensing performance. (a) $\Delta R/R_0$ of the DA-Hydrogel with the compressive strain under various conditions. (b) Gauge factor and linearity of the DA-Hydrogel across various conditions. (c) $\Delta R/R_0$ of the DA-Hydrogel under loading-unloading cycles at the compressive strain of 50% across diverse environmental conditions. (d) $\Delta R/R_0$ of the DA-Hydrogel under loading-unloading cycles at the compressive strains of 10%, 30%, and 50%. (e) $\Delta R/R_0$ of the DA-Hydrogel throughout 1000 stretching-releasing cycles with the compressive strain of 50%. (f) Response/recovery time of the DA-Hydrogel at the compressive strain of 50% at room temperature.

measured external pressure and release motions, demonstrating stable sensing capabilities under thermal exposure (Figure 6b; Figure S19). DA-Hydrogel maintained its sensing capability at −20°C, successfully capturing both pressure and release motions (Figure S20). In contrast, ST-Hydrogel was unsuitable for pressure sensing, as it experienced water loss at elevated temperatures and freezing at lower temperatures, both of which severely compromised its mechanical integrity and electrical properties (Figure S21 and Movie S5). These results underscore the DA-Hydrogel's superior thermal management and stable strain sensing performance, making it a highly promising material for wearable sensors capable of operating in various environments.

DA-Hydrogels effectively track human movements in real-time, which is crucial for biomechanics and kinesiology [69–75]. These features have implications for healthcare and performance monitoring, including injury prevention [76], pain management [77], and precise gait analysis [78]. To demonstrate the application of the hydrogel in motion tracking, we developed several prototypes capable of measuring strain changes in various body joints (e.g., foot, elbow, wrist, and knee) (Figure 6c). The hydrogel exhibited consistent and significant resistance changes in response to deformations caused by diverse body movements (Figure 6d). Remarkably, this performance remained stable even after exposure to various conditions, attributed to the hydrogel's unique properties, including environmental stability and stable strain

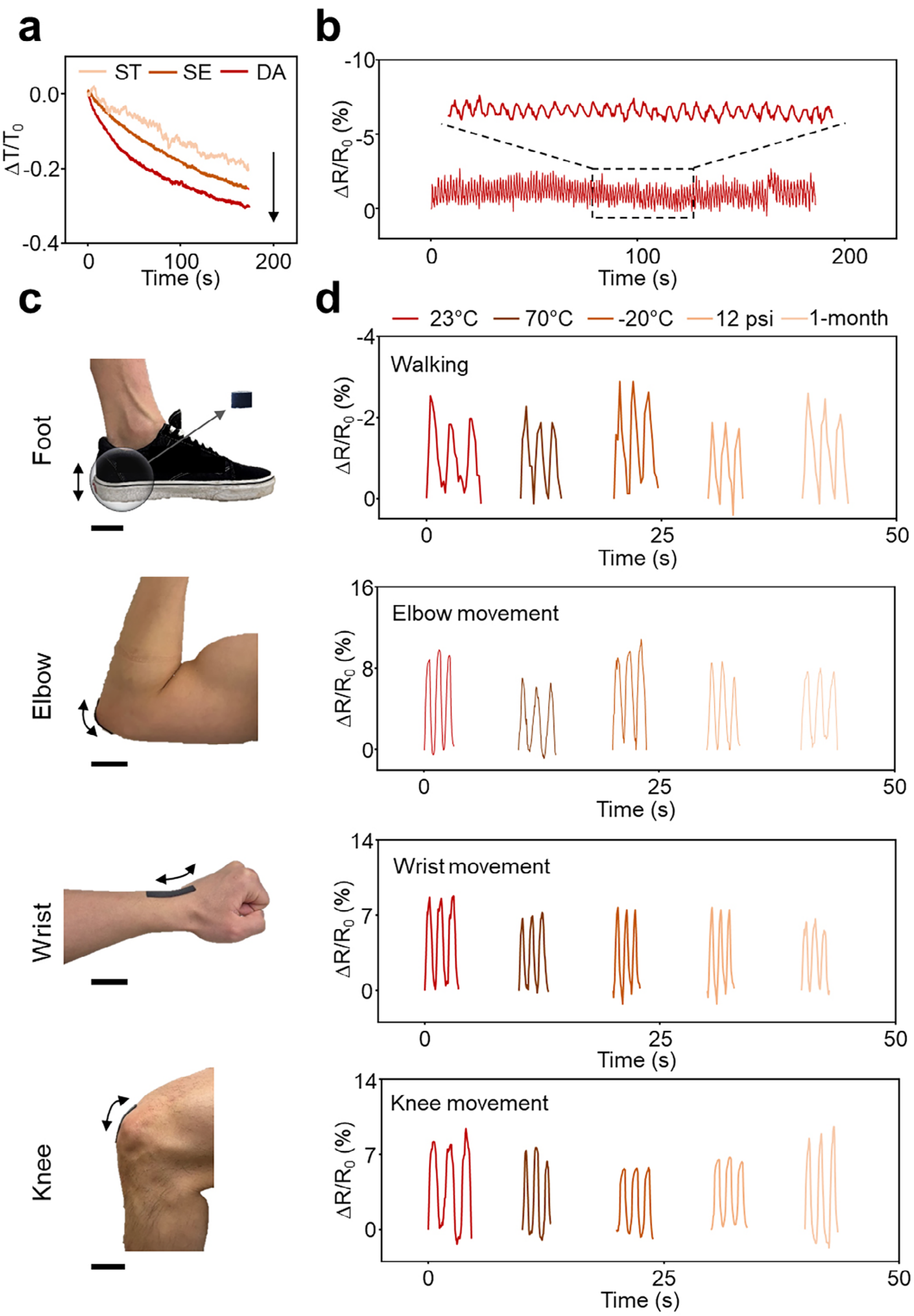

FIGURE 6 | Proof-of-concept demonstrations in wearable sensing. (a) Thermal management of ST-, SE-, and DA-Hydrogels. (b) Sensing performance of the DA-Hydrogel. (c) Photographs of the DA-Hydrogel attached to different body parts. Scale bar, 4 cm. (d) Detection of human motion from the different body parts.

sensing performance. Skin irritation tests confirmed their safety for use on the skin (Figure S22). In the tests, the hydrogel and 3 M tapes were applied to human skin for approximately 10 min and then removed, with untreated bare skin serving as a control. The 3 M tapes caused visible irritation, indicated by a hemoglobin level of 1.8 mg/mL, whereas the hydrogel showed no irritation, with a hemoglobin level of 1.5 mg/mL. These findings highlight the hydrogel's superior biocompatibility. Detailed protocols and results of the skin irritation tests are provided in the Experimental Section.

3 | Conclusion

This study introduces a multiscale engineering strategy for developing hydrogels with enhanced thermal conductivity, mechanical strength, and environmental resilience. Inspired by the design motifs of spider silk, the integration of compact structures across multiple scales has significantly improved hydrogel performance. This multiscale approach provides a versatile framework for designing materials with exceptional properties, critical for applications in wearable sensors and beyond. By advancing the understanding of the relationship between hierarchical structures and hydrogel performance, this work establishes a strong foundation for the rational design of biomimetic hydrogels. The principles demonstrated here are broadly applicable to other material systems, offering opportunities to enhance performance and expand applications in fields such as electronics, soft robotics, energy, and healthcare. While these results are promising, further efforts are required to scale up production and integrate these hydrogels into emerging technologies, including devices, electronics and energy storage, to facilitate their transition from lab-scale innovations to practical industrial applications. This work not only advances the field of biomimetic materials but also paves the way for transformative innovations across industries, including wearable sensors, electronics, soft robotics, energy systems, and biomedical technologies.

4 | Experimental Section

4.1 | Fabrication of Hydrogels

DA-Hydrogels were synthesized using a combination of freeze-thaw and dry-annealing methods, as illustrated in Figure S2. We selected PVA (Mw: 146 000-186 000) as the base polymer for its tunable microstructure, crystallinity, and intermolecular interactions [79]. The synthesis of SE-Hydrogel began by heating a mixture of 4 g deionized water and ethylene glycol (Fisher Chemical) to 95°C, followed by the dissolution of 0.31 g hydroxypropyl cellulose (HPC, Sigma–Aldrich) with continuous stirring for 1 h. Once fully dissolved, 1 g of PVA was added to the solution and stirred for an additional h to achieve homogeneity. Subsequently, 1 g of PEDOT:PSS was incorporated into the PVA-HPC solution, with stirring maintained for another hour. Lastly, 2 g of glycerol (Sigma-Aldrich) was added, and the mixture was stirred until a uniform hydrogel precursor was obtained. The prepared solution was transferred into a pre-cleaned mold and allowed to rest at room temperature for 1 min to eliminate air bubbles. To ensure sterility and prevent contamination, a glass cover, thoroughly cleaned with acetone, isopropanol, and deionized water, was placed over the mold. The solution underwent a freeze-thaw process to enhance its mechanical and electrical properties. Specifically, the hydrogel solution was frozen at −20°C overnight, followed by thawing at 25°C for 3 h. After the thawing process, the hydrogel was carefully demolded and trimmed to the desired dimensions, yielding the SE-hydrogel. The hydrogel formulation consisted of 1 g of PVA, 10 g of deionized water, and 1 g of PEDOT:PSS, while the ST-Hydrogel included an additional 0.31 g of HPC along with the same components, and both were synthesized using an identical protocol. There is no evidence of new chemical bond formation between PVA and HPC, as indicated by the absence of additional peaks in the FTIR spectra (Figure S23) [80]. While the inclusion of HPC improved the mechanical strength of the hydrogels, excessive amounts were found to reduce the strain, with the optimal concentration determined to be 2.5 wt.% HPC (Figure S24). The dry annealing process was performed by placing the freeze-thawed and trimmed specimens between two glass substrates, followed by heating at 60°C for over 1 h. After the initial stage, one glass substrate was removed to expose one side of the specimen, allowing for additional annealing. The annealing procedure was carried out overnight, resulting in the final DA-Hydrogel. Dry annealing of the SE-Hydrogel, which initially contains approximately 40.5 wt.% water, significantly reduces its water content. Specifically, dry annealing results in a consistent weight reduction of 39.4% (Figure S25a), primarily attributed to water loss. The dry annealing promotes PVA crystallization, which disrupts the electrical conductive pathways and consequently reduces the electrical conductivity (Figure S25b) [81]. Hydrogels without HPC and PEDOT:PSS, prepared by freeze-thaw and dry annealing, exhibited a thermal conductivity of 0.6 W/m·K, highlighting the role of their hydrogen bonding with PVA in enhancing thermal conductivity (Figure S26) [82, 83].

4.2 | Thermal Characterization

The thermal conductivities of the samples were measured using a 1D steady-state method in accordance with ASTM D5470 (Figure S3a) [84]. The reference material used was stainless steel, with a thermal conductivity of 16.3 W/m·K. The test sample was positioned between two metal blocks vertically installed in the cylindrically-shaped test section, which was well-insulated to minimize heat loss to the surroundings. Heat was applied to the upper metal block via a film heater, while the temperature of the lower metal block was maintained using a cooling system. To minimize thermal contact resistance between the sample and the metal blocks, pressure was applied during the measurement. Moreover, insulating materials (polyethylene foam, Techlon, with a thermal conductivity of 0.036 W/m·K) were installed in the test section to minimize heat loss during the measurements. The temperatures at six locations on the sample were monitored using type T thermocouples. Thermal conductivities were determined using the Fourier heat conduction equation as shown below:

$$\kappa = \frac{0.5 \times \left(q''_U + q''_L\right) \times |d_3 - d_4|}{|T_3 - T_4|} \tag{1}$$

$$q''_U = \frac{\kappa_s \times |T_1 - T_2|}{|d_1 - d_2|} \tag{2}$$

$$q''_L = \frac{\kappa_s \times |T_5 - T_6|}{|d_5 - d_6|} \tag{3}$$

where k is the calculated thermal conductivity (W/m·K), q“$_{\text{U}}$ and q”$_{\text{L}}$ represent the heat fluxes in the upper and lower parts of the measurement section, d is the location of the temperature measurement, T denotes the temperature of the specific location, κ_s is the thermal conductivity of the reference material (stainless steel, 16.3 W/m·K). The temperature profiles over time for the three types of hydrogels are presented in Figure S3b as shown in the Supporting Information. To intuitively illustrate differences in thermal conductivities, ST-, SE-, and DA-Hydrogels were placed on a flat hot surface set to 80°C. The IR images and temperature profiles were recorded using a thermal infrared camera (FLIR E96 Advanced Thermal Imaging Camera, Teledyne FLIR LLC, Wilsonville, OR).

4.3 | Mechanical Characterization

The mechanical performance of the samples was assessed using a Mark-10 mechanical testing system, which generated stress–strain curves for analysis. Stress was defined as the ratio of the applied force to the cross-sectional area of the specimen, while strain was calculated as the ratio of the elongation to the initial length of the sample. The elastic modulus was determined from the slope of the initial linear region of the stress–strain curve. Toughness, representing the energy required to deform the material, was quantified by integrating the total area under the stress–strain curve. Energy dissipation, reflecting the material's capacity to absorb and release energy, was calculated from the area enclosed within the loading and unloading stress–strain loops.

4.4 | Electrical Characterization

The electrical resistance of the samples was measured using a Keithley 2400 source meter (Tektronix, Inc.). To assess mechanical and electrical performance under diverse conditions, samples were pre-conditioned by subjecting them to specific environments prior to testing at room temperature. These conditions included exposure to −20°C or 70°C, vacuum treatment at 12 psi for 12 h, and storage in ambient air for one month. Gauge factor is defined by the following Equation (4):

$$GF = (\Delta \mathrm{R}/\mathrm{R}_0)/\varepsilon \tag{4}$$

where R_0, $\Delta\mathrm{R}$, and ε are the initial resistance before stretching, the change in resistance under stretching, and the applied strain, respectively.

4.5 | Structural Analysis

The hydrogels underwent microstructural analysis using high-resolution scanning electron microscopy (SEM, S-4800; Hitachi, Inc.) following a 48-h freeze-drying process with a Scientific Pro Freeze Dryer (HR7000-M, Harvestright, LLC).

4.6 | XRD Analysis

Crystallinity and crystallite size were characterized via XRD using a Panalytical Empyrean system with Cu Kα radiation at 45 kV and 40 mA. The degree of crystallinity was calculated as the ratio of the crystalline component to the sum of the crystalline and amorphous components derived from deconvolution. Crystallite size (D) was determined using the Scherrer Equation (5):

$$D = \frac{K\lambda}{(FWHM) \times cos\theta} \tag{5}$$

where K is the equipment constant (0.89) and λ is the wavelength of X-ray (1.54178 Å). FWHM represents the full width at half maxima of the peak and θ is the diffraction angle.

4.7 | FTIR Spectroscopy

FTIR spectroscopy was performed on a Thermo Nicolet iS50 spectrometer in absorption mode over a wavenumber range of 500–4000 cm^{-1}, with and a resolution of 4 cm^{-1} and 16 scan acquisitions. Samples were carefully positioned to ensure full coverage of the FTIR crystal surface.

4.8 | DSC Analysis

DSC analysis was performed using a DSC 8500 system (PerkinElmer, USA) under a nitrogen atmosphere, with a temperature ramp rate of 10 °C min^{-1}.

4.9 | Motion Detection

All human studies were conducted in accordance with university regulations and were approved by the Institutional Review Board (IRB, protocol #: 202212-009-03). For electrical connections, copper tapes (CST5, Digi-Key) and silicone-covered stranded-core wires (Adafruit, Inc.) were secured to both sides of the samples.

4.10 | Skin Irritation Assessment

Imaging was employed to assess potential skin irritation, with erythema and hemoglobin concentration changes serving as key indicators of inflammation [85]. Hyperspectral line-scan images (hypercubes) were captured using a monochrome camera (GS3-U3-120S6M-C, FLIR) paired with a 23 µm slit and a groove density of 150 mm^{-1}. Illumination was provided by an LED light source (D65, 6,500 K), while a xenon light source, emitting multiple narrow peaks at specific wavelengths, was used for spectrograph calibration. Imaging was conducted with a fixed focal length lens (MVL25M1, Navitar) providing a field of view of 10 mm × 10 mm. RGB images of the same skin area were captured using a smartphone camera (iPhone 11 Pro, Apple). The DA-Hydrogel was applied to the medial antebrachial cutaneous region of the forearm for 10 min. A 3 M tape was attached to the same area for 10 min as a positive control. Images were captured both before and after the test to evaluate changes in hemoglobin content. Data acquisition involved a mechanical linear scan at 0.25 mm increments, with data collected via a custom MATLAB interface. To extract hemodynamic parameters, a tissue reflectance spectral model was applied, incorporating radiative transport theory and approximations such as diffusion, Born, and empirical models. The reflected intensity from the biological tissue was analyzed as a function of wavelength (λ) in the visible spectrum. The spectral range of hyperspectral line-scan data was 380–720 nm, and the spectral resolution $\Delta\lambda$ was 0.5 nm. We make use of a tissue reflectance spectral model to extract key hemodynamic parameters from the ground-truth and recovered hyperspectral data. Light propagation in tissue can be modeled in accordance with the theory of radiative transport and robust approximations (e.g. diffusion, Born, and empirical modeling). Specifically, we conducted parameter extractions using an extensively used empirical modeling method. The intensity reflected from a biological sample can be expressed as a function of λ in the visible range:

$$I_R\,(\lambda) = \left[b_1 \left(\frac{\lambda}{\lambda_0} \right)^{b_2} + b_3 \left(\frac{\lambda}{\lambda_0} \right)^{-4} \right] \exp\left[-b_4 \times \left\{ b_5 \times \varepsilon_{HbO_2}(\lambda) + (1 - b_5) \times \varepsilon_{Hb}(\lambda) \right\} \right] \quad (6)$$

where b_1, b_2, and b_3 are associated with the scattering (Mie or Rayleigh) contributions at $\lambda_0 = 800$ nm, $\varepsilon_{HbO2}(\lambda)$ denotes the absorption coefficient of oxygenated hemoglobin (HbO_2), $\varepsilon_{Hb}(\lambda)$ denotes the absorption coefficient of deoxygenated hemoglobin (H_b), b_4 is the hemoglobin concentration multiplied by the optical pathlength, and b_5 is the blood oxygen saturation (sPO_2). Hemoglobin values of all the pixels in the image were averaged to show the bar graph in Figure S22. Specifically, the value of hemoglobin contents multiplied by the optical path length (b4) was utilized to indicate the level of skin irritation by Equation (6). All fitting parameters were computed utilizing the simplex search (Nelder–Mead) algorithm.

4.11 | Statistical Analysis

Data are presented as mean ± standard deviation (SD), with sample sizes of n = 3–4 as specified for each experiment. Statistical analysis was performed using Origin software.

Acknowledgements

This work was partly supported by the Korea Institute for Advancement of Technology (KIAT) grant, funded by the Korea Government (MOTIE) (Global Industrial Technology Cooperation Center support program and International Cooperative R&D program (P0028319)). C.H.L. acknowledges support from the Leslie A. Geddes Endowment. H.J. acknowledges funding support from Korean Institute for Advancement of Technology (KIAT) grant funded by the Korea Government (MOTIE) (RS-2024-00435157, Human Resource Development Program for Industrial Innovation (Global)). H.L. acknowledges the support from the National Science Foundation (United States) under the grant ECCS-1944480. K.J.W. participated in this project and assisted with experiments during a summer internship at Purdue University.

Conflicts of Interest

The authors declare no conflict of interest.

Data Availability Statement

The data that support the findings of this study are available from the corresponding author upon reasonable request.

References

1. Y. Dai, S. Wai, P. Li, et al., "Soft Hydrogel Semiconductors with Augmented Biointeractive Functions," *Science* 386 (2024): 431–439.

2. Y. Shin, H. S. Lee, J.-U. Kim, et al., "Functional-Hydrogel-Based Electronic-Skin Patch for Accelerated Healing and Monitoring of Skin Wounds," *Biomaterials* 314 (2025): 122802.

3. S. Hong, T. Park, J. Lee, et al., "Rapid self-healing hydrogel with ultralow electrical hysteresis for wearable sensing," *ACS Sensors* 9 (2024): 662.

4. Z. Zhang, K. Li, Y. Li, Q. Zhang, H. Wang, and C. Hou, "Dual-function wearable hydrogel optical fiber for monitoring posture and sweat pH," *ACS Sensors* 9 (2024): 3413–3422.

5. X.-Q. Wang, K. H. Chan, W. Lu, et al., "Macromolecule Conformational Shaping for Extreme Mechanical Programming of Polymorphic Hydrogel Fibers," *Nature Communications* 13 (2022): 3369.

6. Y. Luo, M. R. Abidian, J.-H. Ahn, et al., "Technology Roadmap for Flexible Sensors," *ACS Nano* 17 (2023): 5211.

7. X. Qiao, Y. Cai, Z. Kong, Z. Xu, and X. Luo, *ACS Sensors* 2023, 8, 2834–2842.

8. W. Shi, S. Jang, M. A. Kuss, et al., "Digital Light Processing 4D Printing of Poloxamer Micelles for Facile Fabrication of Multifunctional Biocompatible Hydrogels as Tailored Wearable Sensors," *ACS Nano* 18 (2024): 7580.

9. Y. Dai, J. Nolan, E. Madsen, et al., "Wearable Sensor Patch with Hydrogel Microneedles for in Situ Analysis of Interstitial Fluid," *ACS Applied Materials & Interfaces* 15 (2023): 56760.

10. H. Wei, D. Kong, T. Li, et al., "Solution-Processable Conductive Composite Hydrogels with Multiple Synergetic Networks toward Wearable Pressure/Strain Sensors," *ACS Sensors* 6 (2021): 2938–2951.

11. J. Ma, W. Du, Z. Chen, W. Wang, and L. Zhang, "Preparation of Graphene-Based Hydrogel Thermal Interface Materials with Excellent Heat Dissipation and Mechanical Properties," *Macromolecular Materials and Engineering* 308 (2023): 2200332.

12. J. Liu, H. Zhai, J. Li, Y. Li, and Z. Liu, "Enhancing wearable electronics through thermal management innovations," *Wearable Electronics* 1 (2024) 160–179.

13. Z. Shen and J. Feng, "Highly Thermally Conductive Composite Films Based on Nanofibrillated Cellulose in Situ Coated with a Small Amount of Silver Nanoparticles," *ACS Applied Materials & Interfaces* 10 (2018): 24193.

14. L. Sheng, Y. Wang, X. Wang, C. Han, and Z. Chen, "A Thermal Management Strategy for Electronic Devices Based on Copper Double Skin Inspired Hydrogel," *International Journal of Heat and Mass Transfer* 206 (2023): 123946.

15. A. Yazdan, J.-Z. Wang, B.-K. Hu, et al., "Boron Nitride/Agarose Hydrogel Composites with High Thermal Conductivities," *Rare Metals* 39 (2020): 375–382.

16. Z. Li, D. Pan, Z. Han, et al., "Boron Nitride Whiskers and Nano Alumina Synergistically Enhancing the Vertical Thermal Conductivity of Epoxy-cellulose Aerogel Nanocomposites," *Advanced Composites and Hybrid Materials* 6 (2023): 224.

17. Q. Chen, K. Yang, Y. Feng, et al., "Recent Advances in Thermal-conductive Insulating Polymer Composites with Various Fillers," *Composites Part A: Applied Science and Manufacturing* 178 (2023): 107998.

18. L. Xing, C. Hu, Y. Zhang, X. Wang, L. Shi, and R. Ran, "A Mechanically Robust Double-network Hydrogel with High Thermal Responses via Doping Hydroxylated Boron Nitride Nanosheets," *Journal of Materials Science* 54 (2019): 3368–3382.

19. L. Jing, H. Li, R. Y. Tay, et al., "Biocompatible Hydroxylated Boron Nitride Nanosheets/Poly(vinyl alcohol) Interpenetrating Hydrogels with Enhanced Mechanical and Thermal Responses," *ACS Nano* 11 (2017): 3742–3751.

20. T. Meng, P. Zhang, H. Zhong, et al., "Phonon Transport in Supramolecular Polymers Regulated by Hydrogen Bonds," *Nano Letters* 24 (2024): 14095–14101.

21. X. Xie and D. Yang, "Self-healing Thermally Conductive Polymer Composites Based on Polyvinyl Alcohol with Dynamic Borate Ester and Hydrogen Bonds," *Composites Part A: Applied Science and Manufacturing* 181 (2024): 108131.

22. Q. Wei and D. Yang, “A Self-healing Polyvinyl Alcohol-based Composite with High Thermal Conductivity and Excellent Mechanical Properties,” *Composites Communications* 39 (2023): 101561.

23. M. Qin, Y. Huo, G. Han, et al., “Three-dimensional Boron Nitride Network/Polyvinyl Alcohol Composite Hydrogel with Solid-Liquid Interpenetrating Heat Conduction Network for Thermal Management,” *Journal of Materials Science & Technology* 127 (2022): 183.

24. F. Jiang, S. Cui, N. Song, L. Shi, and P. Ding, “Hydrogen Bond-Regulated Boron Nitride Network Structures for Improved Thermal Conductive Property of Polyamide-imide Composites,” *ACS Applied Materials & Interfaces* 10 (2018): 16812.

25. H. Zheng, K. Wu, Y. Zhan, K. Wang, and J. Shi, “High Intrinsic Thermal Conductive Polymer Films by Engineered Interchain Hydrogen Bond Interactions,” *Journal of Polymer Science* 61 (2023): 1622.

26. Y. Park, M. You, J. Shin, et al., “Thermal Conductivity Enhancement in Electrospun Poly(vinyl alcohol) and Poly(vinyl alcohol)/Cellulose Nanocrystal Composite Nanofibers,” *Scientific Reports* 2019, 9, 3026.

27. J. Zhang, C. Tang, Q. Kong, et al., “Strong and Tough Polyvinyl Alcohol Hydrogels with High Intrinsic Thermal Conductivity,” *Soft Science* 5 (2025): 9.

28. S. Hong, T. Yu, Z. Wang, and C. H. Lee, “Biomaterials for Reliable Wearable Health Monitoring: Applications in Skin and Eye Integration,” *Biomaterials* 314 (2025): 122862.

29. Z. Han, P. Wang, Y. Lu, Z. Jia, S. Qu, and W. Yang, “A Versatile Hydrogel Network–repairing Strategy Achieved by the Covalent-Like Hydrogen Bond Interaction,” *Science Advances* 8 (2022): abl5066.

30. H. Zhang, Z. Liu, J. Mai, et al., “A Smart Design Strategy for Super-Elastic Hydrogel with Long-Term Moisture, Extreme Temperature Resistance, and Non-Flammability,” *Advanced Science* 8 (2021): 2100320.

31. J. Li, S. Li, J. Huang, et al., “Spider Silk-Inspired Artificial Fibers,” *Advanced Science* 9 (2022): 2103965.

32. C. Fu, Y. Wang, J. Guan, X. Chen, F. Vollrath, and Z. Shao, “Cryogenic Toughness of Natural Silk and a Proposed Structure–Function Relationship,” *Materials Chemistry Frontiers* 3 (2019): 2507.

33. L. Zhang, T. Chen, H. Ban, and L. Liu, “Hydrogen Bonding-assisted Thermal Conduction in β-sheet Crystals of Spider Silk Protein,” *Nanoscale* 6 (2014): 7786.

34. T. Giesa, M. Arslan, N. Pugno, and M. Buehler, “Nanoconfinement of Spider Silk Fibrils Begets Superior Strength, Extensibility and Toughness,” *Nature Precedings* (2011): 1.

35. L. Gu, Y. Jiang, and J. Hu, “Scalable Spider-Silk-like Supertough Fibers Using a Pseudoprotein Polymer,” *Advanced Materials* 31 (2019): 1904311.

36. X. Huang, G. Liu, and X. Wang, “New Secrets of Spider Silk: Exceptionally High Thermal Conductivity and Its Abnormal Change under Stretching,” *Advanced Materials* 24 (2012): 1482.

37. J. J. Paik, B. Jang, S. Nam, and L. J. Guo, “A Transparent Poly(vinyl alcohol) Ion-Conducting Organohydrogel for Skin-Based Strain-Sensing Applications,” *Advanced Healthcare Materials* 12 (2023): 2300076.

38. Y. Chen, J. Li, J. Lu, M. Ding, and Y. Chen, “Synthesis and Properties of Poly(vinyl alcohol) Hydrogels with High Strength and Toughness,” *Polymer Testing* 108 (2022): 107516.

39. S. Hong, J. Park, S. G. Jeon, et al., “Monolithic Bi1.5Sb0.5Te3 Ternary Alloys with a Periodic 3D Nanostructure for Enhancing Thermoelectric Performance,” *Journal of Materials Chemistry B* 5 (2017): 8974.

40. K. Kim, J. Park, S. Hong, et al., “Anomalous Thermoelectricity of Pure ZnO from 3D Continuous Ultrathin Nanoshell Structures,” *Nanoscale* 10 (2018): 3046.

41. S. Lin, X. Liu, J. Liu, et al., “Anti-fatigue-fracture Hydrogels,” *Science Advances* 5 (2019): aau8528.

42. F. Wu, J. Gao, Y. Xiang, and J. Yang, “Enhanced Mechanical Properties of PVA Hydrogel by Low-Temperature Segment Self-Assembly vs. Freeze–Thaw Cycles,” *Polymers* 15 (2023): 3782.

43. A. Xiang, C. Lv, and H. Zhou, “Changes in Crystallization Behaviors of Poly(Vinyl Alcohol) Induced by Water Content,” *Journal of Vinyl and Additive Technology* 26 (2020): 613.

44. Y. Guo, K. Ruan, X. Shi, X. Yang, and J. Gu, “Factors Affecting Thermal Conductivities of the Polymers and Polymer Composites: a Review,” *Composites Science and Technology* 193 (2020): 108134.

45. J. W. Zhang, D. D. Dong, X. Y. Guan, et al., “Physical Organohydrogels with Extreme Strength and Temperature Tolerance,” *Frontiers in Chemistry* 8 (2020): 102.

46. Y. Song, S. Zhang, J. Kang, J. Chen, and Y. Cao, “Water Absorption Dependence of the Formation of Poly(vinyl alcohol)-iodine Complexes for Poly(vinyl alcohol) Films,” *RSC Advances* 11 (2021): 28785–28796.

47. R. Kumar and A. Parashar, “Effect of the Degree of Polymerization and Water Content on the Thermal Transport Phenomena in PEGDA Hydrogel: a Molecular-dynamics-based Study,” *Physical Chemistry Chemical Physics* 25 (2023): 18960.

48. N. Tang, Z. Peng, R. Guo, et al., “Thermal Transport in Soft PAAm Hydrogels,” *Polymers* 9 (2017): 688.

49. J. Zhou, S. Lin, H. Zeng, et al., “Dynamic Intermolecular Interactions through Hydrogen Bonding of Water Promote Heat Conduction in Hydrogels,” *Materials Horizons* 7 (2020): 2936.

50. S. Xu, S. Cai, and Z. Liu, “Thermal Conductivity of Polyacrylamide Hydrogels at the Nanoscale,” *ACS Applied Materials & Interfaces* 10 (2018): 36352.

51. Y. Xie, Z. Li, Y. Zhang, Y. Lu, J. Zhang, and L. Zong, “Ultralight, Heat-Insulated, and Tough PVA Hydrogel Hybridized with SiO 2 @Cellulose Nanoclaws Aerogel via the Synergy of Hydrophilic and Hydrophobic Interfacial Interactions,” *Small* 19 (2023): 2303044.

52. Z. Shen, J. Ma, Y. Cai, et al., “Low-water-content polyelectrolyte hydrogels inspired by human epidermal stratum corneum,” *Cell Reports Physical Science* 4 (2023): 101741.

53. K. Hu, Z. Zhao, Y. Wang, et al., “A Tough Organohydrogel-based Multiresponsive Sensor for a Triboelectric Nanogenerator and Supercapacitor toward Wearable Intelligent Devices,” *Journal of Materials Chemistry A* 10 (2022): 12092.

54. Y. Shi, J. Liu, J. Li, D. Xiong, and D. Dini, “Improved Mechanical and Tribological Properties of PAAm/PVA Hydrogel-Ti6Al4V Alloy Configuration for Cartilage Repair,” *Journal of Polymer Research* 29 (2022): 515.

55. Y. Zhu, W. Lu, Y. Guo, Y. Chen, Y. Wu, and H. Lu, “Biocompatible, Stretchable and Mineral PVA–gelatin–nHAP Hydrogel for Highly Sensitive Pressure Sensors,” *RSC Advances* 8 (2018): 36999–37007.

56. D. H. Oh, P. Le Thi, and K. D. Park, “Injectable Dual Fenton/Enzymatically Cross-Linked Double-Network Hydrogels Based on Acrylic/Phenolic Polymers with Highly Reinforced and Tunable Mechanical Properties,” *ACS Applied Bio Materials* 7 (2024): 5702.

57. C. Zhou, S. Yuan, T. Dai, S. Zhou, H. Zou, and P. Liu, “Environment-adaptable PAM/PVA Semi-IPN Hydrogels Reinforced by GO for High Electromagnetic Shielding Performance,” *Polymer* 253 (2022): 125028.

58. C. Xiang, X. Zhang, J. Zhang, et al., “A Porous Hydrogel with High Mechanical Strength and Biocompatibility for Bone Tissue Engineering,” *Journal of Functional Biomaterials* 13 (2022): 140.

59. F. Mo, Y. Huang, Q. Li, et al., “A Highly Stable and Durable Capacitive Strain Sensor Based on Dynamically Super-Tough Hydro/Organo-Gels,” *Advanced Functional Materials* 31 (2021): 2010830.

60. X. P. Morelle, W. R. Illeperuma, K. Tian, R. Bai, Z. Suo, and J. J. Vlassak, "Highly Stretchable and Tough Hydrogels below Water Freezing Temperature," *Advanced Materials* 30 (2018): 1801541.

61. F. Chen, D. Zhou, J. Wang, et al., "Rational Fabrication of Anti-Freezing, Non-Drying Tough Organohydrogels by One-Pot Solvent Displacement," *Angewandte Chemie* 130 (2018): 6678.

62. Y. Liu, H. Yu, G. Zhou, and M. Peng, "Superhydrophobic, Anti-Freezing and Multi-Cross-Linked Wearable Hydrogel Strain Sensor for Underwater Gesture Recognition," *ACS Sensors* 9 (2024): 4617–4625.

63. Z. Pei, Z. Yuan, C. Wang, et al., "A Flexible Rechargeable Zinc–Air Battery with Excellent Low-Temperature Adaptability," *Angewandte Chemie International Edition* 59 (2020): 4793.

64. B. Ying, R. Z. Chen, R. Zuo, J. Li, and X. Liu, "An Anti-Freezing, Ambient-Stable and Highly Stretchable Ionic Skin with Strong Surface Adhesion for Wearable Sensing and Soft Robotics," *Advanced Functional Materials* 31 (2021): 2104665.

65. Y. Zhao, N. Yang, X. Chu, et al., "Wide-Humidity Range Applicable, Anti-Freezing, and Healable Zwitterionic Hydrogels for Ion-Leakage-Free Iontronic Sensors," *Advanced Materials* 35 (2023): 2211617.

66. S. Hong, T. Park, J. Lee, et al., "Tough Conductive Organohydrogel for Wearable Sensing in Extreme Environmental Conditions," *Advanced Materials Technologies* 9 (2024): 2301398.

67. R. Wang, C. Liu, Z. Li, Y. Li, and X. Yu, "Ultra-stretchable, adhesive, conductive, and antifreezing multinetwork borate ester-based hydrogel for wearable strain sensor and VOC absorption," *ACS Sensors* 9 (2024): 5322–5332.

68. S. Hong, J. Lee, T. Park, et al., "Spider Silk-Inspired Conductive Hydrogels for Enhanced Toughness and Environmental Resilience via Dense Hierarchical Structuring," *Advanced Science* 12 (2025): 2500397.

69. R. Yin, D. Wang, S. Zhao, Z. Lou, and G. Shen, "Wearable Sensors-Enabled Human–Machine Interaction Systems: from Design to Application," *Advanced Functional Materials* 31 (2021): 2008936.

70. L.-W. Lo, J. Zhao, H. Wan, Y. Wang, S. Chakrabartty, and C. Wang, "A Soft Sponge Sensor for Multimodal Sensing and Distinguishing of Pressure, Strain, and Temperature," *ACS Applied Materials & Interfaces* 14 (2022): 9570.

71. M. D. Bartlett, E. J. Markvicka, and C. Majidi, "Rapid Fabrication of Soft, Multilayered Electronics for Wearable Biomonitoring," *Advanced Functional Materials* 26 (2016): 8496.

72. L. Liu, T. Luo, X. Kuang, et al., "Highly Stretchable and Multimodal MXene/CNTs/TPU Flexible Resistive Sensor with Hierarchical Structure Inspired by Annual Ring for Hand Rehabilitation," *ACS Sensors* 9 (2024): 2476–2487.

73. T. Park, T. I. Mahmud, J. Lee, et al., "A Machine-learning-enabled Smart Neckband for Monitoring Dietary Intake," *PNAS Nexus* 3 (2024): pgae156.

74. S. Hong, H. Zhang, J. Lee, et al., "Spongy Ag Foam for Soft and Stretchable Strain Gauges," *ACS Applied Materials & Interfaces* 16 (2024): 26613–26623.

75. T. Chang, S. Akin, S. Cho, et al., "In Situ Spray Polymerization of Conductive Polymers for Personalized E-textiles," *ACS Nano* 17 (2023): 22733.

76. C. Tan, Z. Dong, Y. Li, et al., "A High Performance Wearable Strain Sensor with Advanced Thermal Management for Motion Monitoring," *Nature Communications* 11 (2020): 3530.

77. N. Qaiser, F. Al-Modaf, S. M. Khan, S. F. Shaikh, N. El-Atab, and M. M. Hussain, "A Robust Wearable Point-of-Care CNT-Based Strain Sensor for Wirelessly Monitoring Throat-Related Illnesses," *Advanced Functional Materials* 31 (2021): 2103375.

78. M. Amit, L. Chukoskie, A. J. Skalsky, H. Garudadri, and T. N. Ng, "Flexible Pressure Sensors for Objective Assessment of Motor Disorders," *Advanced Functional Materials* 30 (2020): 1905241.

79. W. X. Waresindo, H. R. Luthfianti, A. Priyanto, et al., "Freeze–thaw Hydrogel Fabrication Method: Basic Principles, Synthesis Parameters, Properties, and Biomedical Applications," *Materials Research Express* 10 (2023): 024003.

80. Z. Wang, X. Xu, Y. Xu, W. Lin, and Z. Peng, "A Ternary Heterogeneous Hydrogel with Strength Elements for Resilient, Self-healing, and Recyclable Epidermal Electronics," *npj Flexible Electronics* 6 (2022): 51.

81. Y.-W. Kim, J.-M. Park, C. S. Park, et al., "Anisotropically Conductive Hydrogels with Directionally Aligned PEDOT:PSS in a PVA Matrix," *ACS Applied Materials & Interfaces* 16 (2024): 4013.

82. N. Lu, R. Na, L. Li, et al., "Rational Design of Antifreezing Organohydrogel Electrolytes for Flexible Supercapacitors," *ACS Applied Energy Materials* 3 (2020): 1944.

83. T. Gregorio, D. Mombrú, M. Romero, R. Faccio, and Á. W. Mombrú, "Exploring Mixed Ionic–Electronic-Conducting PVA/PEDOT:PSS Hydrogels as Channel Materials for Organic Electrochemical Transistors," *Polymers* 16 (2024): 1478.

84. C. S. Heu, S. W. Kim, K.-S. Lee, and D. R. Kim, "Fabrication of Three-dimensional Metal-Graphene Network Phase Change Composite for High Thermal Conductivity and Suppressed Subcooling Phenomena," *Energy Conversion and Management* 149 (2017): 608.

85. Y. Ji, S. M. Park, S. Kwon, et al., "mHealth Hyperspectral Learning for Instantaneous Spatiospectral Imaging of Hemodynamics," *PNAS Nexus* 2, no. 2 (2023): pgad111.

Supporting Information

Additional supporting information can be found online in the Supporting Information section.

Supporting file: admi70350-sup-0001-SuppMat.docx **Supplemental Movie 1**: admi70350-sup-0002-MovieS1.mp4 **Supplemental Movie 2**: admi70350-sup-0003-MovieS2.mp4 **Supplemental Movie 3**: admi70350-sup-0004-MovieS3.mp4 **Supplemental Movie 4**: admi70350-sup-0005-MovieS4.mp4 **Supplemental Movie 5**: admi70350-sup-0006-MovieS5.mp4